In-situ activation of self-supported 3D hierarchically porous Ni_3S_2 films grown on nanoporous copper as excellent pH-universal electrocatalysts for hydrogen evolution reaction

C. Yang[a], M. Y. Gao[a], Q. B. Zhang[a,b*], J. R. Zeng[a], X. T. Li[a], and A. P. Abbott[c]

[a] Key Laboratory of Ionic Liquids Metallurgy, Faculty of Metallurgical and Energy Engineering, Kunming University of Science and Technology. Kunming, 650093, P.R. China

[b] State Key Laboratory of Complex Nonferrous Metal Resources Cleaning Utilization in Yunnan Province, Kunming 650093, China

[c] Department of Chemistry, University of Leicester, Leicester, LE1 7RH, UK

Abstract

The exploitation of low-cost, stable, and highly active electrocatalysts based on earth-abundant metals for hydrogen evolution reaction (HER) is crucial for developing renewable energy techniques. In this work, we report a facile synthesis strategy for *in-situ* fabrication of 3D hierarchically porous Ni_3S_2 films on a nanoporous copper substrate (Ni_3S_2@NPC) by unusual galvanic replacement reaction in the Ethaline-based deep eutectic solvent (DES) under a normal atmosphere. The self-supported nanoporous Ni_3S_2@NPC electrode is binder- free and exhibits good structural integrity with high conductivity. A mild evolution of bulk gas bubbles (H_2-O_2 gas mixture) is proved to drive an *in-situ* structure rearrangement process of the Ni_3S_2@NPC and results in substantial increases in the HER activity. The activated Ni_3S_2@NPC (a-Ni_3S_2@NPC) electrode can serve as a highly efficient and stable electrocatalyst for the HER in water over a wide pH range. Significantly, it displays high-performance HER catalytic activity in acidic media with robust durability over 111 h and functions well under alkaline and neutral conditions. Such a superior catalytic performance of the a-Ni_3S_2@NPC is mainly due to the unique hierarchically nanoporous architectures and the synergetic effects in it caused by the restructuring NPC skeletons and active components. Our work offers a generic strategy for design and fabrication of many other self-supported transition metal sulfide and phosphide based HER electrocatalysts, and uncovers a new O_2-induced electrochemical self-activation mechanism for improving the activity of catalysts.

Keywords: Nickel sulfide; Nanoporous; Deep eutectic solvents; Galvanic replacement reaction; Hydrogen evolution reaction

*Corresponding author. Tel: +86-871-65162008; fax: +86-871-65161278.

E-mail address: qibozhang@kmust.edu.cn (Q.B. Zhang)

1. Introduction

The increasing conflict between the increased energy demand and environmental degradation induced by fossil fuel combustion have spawned significant interest in seeking highly effective, clean and renewable alternative energy sources.[1-3] As an abundant and carbon-free fuel, hydrogen offers ultrahigh calorific value with zero CO_2 emission,[4-6] which has been considered as the ideal candidate to substitute for carbon-based fuels in the future.[7, 8] Electrochemical splitting of water driven by renewable electric power provides a flexible and sustainable way to produce high purity hydrogen.[9-11] Practical operation of electrolytic water splitting requires effective catalysts to promote the hydrogen evolution reaction (HER), due to its intrinsic sluggish kinetics. Pt-based materials are identified as the most effective HER catalysts; however, the high cost and low abundance significantly limits their large-scale application.[12] Development of highly efficient, low-cost, noble-metal-free HER catalysts is therefore needed. Additionally, to meet different applications, catalysts that function well over a wide pH range are highly regarded. For instance, water-splitting devices based on proton exchange membrane (PEM) technology demand catalysts that function well in acidic conditions;[13] microbial electrolysis cells (MEC) needs catalysts operating in neutral solution,[14] and basic-stable HER catalysts are required for alkaline water electrolysis under strongly basic media.[15] Although some encouraging progresses have been reported,[16-19] it still remains challenging to design and develop efficient, durable and scalable earth-abundant HER catalysts that can work well at all pH values.

Ni-based alloys have been widely employed as earth-abundant electrocatalysts for hydrogen production due to their substantial HER activity, and extensive efforts have been devoted to maximizing their catalytic activity and durability.[20] In addition, nickel coupled with non-metals (B, P, N, etc.) and chalcogenides (S, Se, Te) have shown high-performance catalytic activity.[21] Among them, nickel sulfides have been extremely studied as electrocatalysts for the water splitting reaction owing to their abundant resources, intrinsic high activity and good electron transport ability.[22, 23] In most cases, nanostructured catalysts are fabricated to ensure a large surface area, sufficient catalytic sites and rapid reaction kinetics. Up-to-now, micro- or nanoarchitectured Ni_3S_2, one of the most important nickel sulfide compounds have been synthesized. They exist in nature as the mineral heazlewoodite, but they have been synthesized with various morphologies such as nanosheets,[23,24] nanowires,[25] nanorods,[26,27] hollow microspheres, [28] and exhibited superior activity and good catalytic stability toward HER as well as overall water splitting in neutral and alkaline media. Unfortunately, few Ni_3S_2-based electrocatalysts show satisfactory HER durability in acidic electrolyte.[23,29] Moreover, the overwhelming majority of these catalysts are prepared by hydrothermal or solvothremal route, which, is tedious and costly, involving high synthesis temperatures, the use of organic solvents,

and/or heat-treatment operating in an inert atmosphere.[22,23,26,30,31] Alternatively, NiS microsphere films have been fabricated as efficient bifunctional catalysts via a direct sulfurization reaction of Ni foam with sulfur powder at a relatively high temperature under an Ar atmosphere.[32] Amorphous Ni-S films prepared by a potentiodynamic deposition approach followed by an annealing process were proved to possess good catalytic activity and stability toward HER in neutral water.[29] Hierarchically porous NiS_x synthesized through galvanostatic electrodeposition from an aqueous electrolyte followed by low-temperature sulfurization displayed an excellent overall alkaline water splitting performance.[33] More recently, we have introduced a novel strategy to prepare nickel nanostructure grown *in-situ* on the copper-based template via an unusual galvanic replacement process in a choline chloride (ChCl)-ethylene glycol (EG)-based deep eutectic solvent (Ethaline). 3D interconnected core/shell nanoporous nickel films are found to grow homogeneously on the nano-ligaments of the nanoporous copper (NPC) template due to the slow reaction kinetics.[34] This self-supported nanoporous nickel film possesses highly active for HER in alkaline solutions, while it is not stable during long-term electrolysis. Inspired by the abovementioned work, with the objective of further improving its activity and durability, we have developed a nickel sulfide (Ni_3S_2) nanoporous film as active earth-abundant catalyst for the HER.

Herein, we report a facile synthesis to directly grow Ni_3S_2 films on a NPC substrate (Ni_3S_2@NPC) as the efficient and stable catalyst for HER in acidic, neutral and basic all-pH value solutions. This Ni_3S_2@NPC catalyst was rationally designed and fabricated in an easy to handle, low-cost, scalable process involving *in-situ* preparation of NPC followed by an unusual galvanic replacement to directly grow Ni_3S_2 films on the NPC template in the Ethaline-based deep eutectic solvent. The self-supported nanoporous Ni_3S_2@NPC electrode exhibits excellent structural integrity and electron conduction. It is interesting to find a mild evolution of gas bubbles resulting in *in-situ* structural rearrangement and activation of the Ni_3S_2@NPC, leading to a significant increase in the HER activity. The activated Ni_3S_2@NPC shows a high electrocatalytic HER activity with small Tafel slopes of 63.5 and 67.5 mV dec^{-1} (iR-corrected) in acidic and alkaline media, respectively, and is found to exhibit good stability. It requires overpotentials of only -91.6 mV in 0.5 M H_2SO_4 and -60.8 mV in 1.0 M KOH, respectively, to deliver a HER current density of 10 mA cm^{-2}. In addition, it also displays super-activity and stable performance under a neutral condition. More importantly, the fabrication approach is applicable for the synthesis of other self-supported nanoporous transition metal sulfide and phosphide based HER electrocatalysts.

2. Results and discussion

The nanoporous Ni_3S_2@NPC electrode was fabricated via a galvanic replacement method in Ethaline using an NPC

template. Nanoporous Ni@NPC was also synthesized for comparison (Figures S1 and S2). As illustrated in Scheme 1, 3D hierarchically nanoporous NPC was used as the starting material to provide a highly porous skeleton for the structure construction. The nanoporous Ni_3S_2 films were grown *in-situ* on the nano-ligaments of the NPC template by simply immersing it in Ethaline with 0.10 M $NiCl_2 \cdot 6H_2O$ and 0.05 M thiourea. A galvanic reaction occurred after 5 h at 353 K which introduces the sulfur through a solvothremal process. The NPC template was originally a dark wine color which turned to bronze for Ni@NPC and black for Ni_3S_2@NPC (Figure S1). A surface rearrangement of the as-prepared Ni_3S_2@NPC was then carried out in strongly acidic or basic media. This *in-situ* self-activation process at the electrode surface is crucial to achieve the self-enhanced HER catalytic activity of the Ni_3S_2@NPC, which is discussed subsequently.

The crystallographic structure of the as-prepared films was determined by X-ray diffraction (XRD) analysis (Figure 1a). The XRD pattern of the NPC template is shown as a reference. The characteristic peaks located at 21.7°, 31.1°,38.3°, 44.3°, 55.1° and 77.6° correspond well to (101), (110), (021), (202), (122) and (223) crystal planes of rhombohedral Ni_3S_2 (JCPSD No.44-1418, a=b=5.745 Å and c=7.135 Å), respectively. In addition, Raman spectra (Figure S3) also verify the formation of a Ni_3S_2 surface alloy on the NPC template. Density functional theory calculations were performed to demonstrate the electronic band structure and relevant density of states of the rhombohedral Ni_3S_2. As shown in Figure 1b-d, these nickel sulfides exist in a cubic-type structure, where the nickel atoms are tetrahedrally bonded to the body-centered cubic sulfur atoms. The calculated density of states suggests the metallic behavior of Ni_3S_2 with predominantly Ni 3d orbitals crossing the Fermi level (Figure 1e). These results reveal the metallic properties of the Ni_3S_2,[23,35,36] which is identified as a highly active HER electrocatalyst (see Supporting Information for more details).

This galvanic replacement reaction can easily be achieved in a normal atmosphere as illustrated in Figure 2a. The resultant self-assembled Ni_3S_2 films exhibit a good adhesion on the NPC substrate, which allows it to resist alternating bending tests (Figure 2b,c). This behavior suggests the high flexibility and robust feature of the Ni_3S_2@NPC. The corresponding scanning electron microscope (SEM) images reveal that the representative hierarchically nanoporous surface of the NPC template, as shown in Figure 2d, is developed into a coral-like nanostructures with well-defined ligaments for Ni@NPC (Figure S2a). In the case of the sulfurization treatment, the nanoporous surface is composed of densely packed nano-ligament (Figure 2e and Figure S4a). The skeleton sizes are found to grow up to 130-170 nm (Ni@NPC) and 200-300 nm (Ni_3S_2@NPC) (insets in Figure S2a and Figure 2e), respectively, after the replacement reaction, indicating a self-assembly process. A well-defined core/shell skeleton structure of the Ni_3S_2@NPC scratched off from the substrate is clearly displayed by the HAADF-STEM image (Figure

2f). The associated cross-sectional compositional line profiles (inset of Figure 2f) reveal the regular distribution of elemental Ni and S at the superface. The selected-area electron diffraction pattern shows well-defined diffraction rings, which indicate the polycrystalline nature of the nano-ligament for the Ni_3S_2@NPC sample (Figure 2g), consistent with the XRD result. The HRTEM image reveals highly resolved lattice fringes with interplanar spacings of 0.23 and 0.28 nm, which correspond to the (021) and (110) planes of Ni_3S_2 (Figure 2h). STEM and the corresponding EDS elemental mapping results clearly show the homogeneous distribution of Ni, S, Cu (from NPC) in the entire skeleton, suggesting the successful formation of a core-shell Ni_3S_2 layer throughout the NPC ligament (Figure 2i-l and Figure S4b-e).

It is worth mentioning that this novel but facile galvanic replacement approach with NPC templates in DESs is also suitable for the fabrication of other self-supported 3D nanostructured M-X (M=Ni, Co; X=S, P) electrodes with corresponding salt precursors. For instance, nanoporous Ni_xP_y, nanorods of Co_2P, nanoflowers of Co_9S_8 and porous nanoparticle packed Co_3S_4 network films were all successfully synthesized (see more details in Figures S5-S7). Interesting morphological differences were obtained, depending on the particular DES chosen for the galvanic reaction, which could be related to the differences in phy-chemical properties, active reaction species and deposition kinetics.[37] Obviously, a more systematic study is needed for a deeper understanding of this galvanic process.

Electrocatalytic measurements were performed in a one-compartment cell using a three-electrode configuration as illustrated in Figure 3a (the optical images are given in Figure S8). Impressively, the HER activity of the as-prepared Ni_3S_2@NPC increases successively during multi-step chronoamperometric (CP) measurements (Figure 3b). According to the corresponding polarization curves recorded at various stages (from 1st to 6th, Figure 3c), the Tafel slope, onset potential and overpotential to drive a current density of 10 mA cm^{-2} of the Ni_3S_2@NPC is found to consistently decrease, while the exchange current density rises steeply after continuous multi-step CP activation, individually in 0.5 M H_2SO_4 (Figure 3d-h). This implies a self-improved activity of the Ni_3S_2@NPC during the electrocatalytic process. Accordingly, the double-layer capacitance value increases after the 5th CP activation, which is approximately 39 times larger than the pristine Ni_3S_2@NPC (Figure 3h and Figure S9). Furthermore, the measured charge transfer resistances, extracted from electrochemical impedance spectroscopy (EIS), as shown in Figure 3i, decrease significantly upon activation, suggesting enhanced charge transport efficiency,[16, 38] which agrees with the visual appearance of hydrogen bubbles generated at the same overpotential of -150 mV on Ni_3S_2@NPC (Figure S10). To further investigate the activated process of the Ni_3S_2@NPC, the morphology and surface property changes were characterized using SEM, AFM and XPS analyses at various activation stages, as shown in Figure 4. The morphological evolution of Ni_3S_2@NPC during *in-situ* activation at different stages is illustrated schematically in

Figure 4a. The microstructure of the catalyst is found to undergo a self-assembly process with the help of bulk gas bubbles evolution, and increasing the activation time results in highly porous surfaces with hierarchical architectures (Figure 4b-e). An obvious surface rearrangement is observed as the relatively flat films of the as-prepared Ni_3S_2@NPC electrode are developed in to highly porous surfaces with a corresponding increase in the peak-to-valley height and surface roughness (AFM-derived, Table S1, Figure 4f-h) after multi-step CP measurements. The associated XPS spectra of the Ni_3S_2@NPC (Figure S11a) show the presence of Ni, S, Cu, C, and O in the as-prepared films consistent with the EDS result (Figure S4a). The high-resolution spectrum of Ni 2p shows trace metallic Ni, coupled with Ni^{2+} and Ni^{3+} on the surface in the form of NiO and Ni_3S_2, respectively (Figure 4j).[39, 40] Curve fitting of the S 2p spectrum fits well with the bridging disulfide S_2^{2-} ligands in Ni_3S_2 (Figure 4k).[40, 41] The Cu 2p spectra show weak substrate signal with dominantly metallic Cu and trace oxidized Cu species (Figure. 4l).[42] In comparison with the fresh sample, the magnitude of Ni 2p spectrum is found to sharply decrease after the first round activation; however, it remains stable during the following activation process, which agrees well with the EDX and ICP-OES results (Figure S12), while the signal for Cu 2p increases (Figure 4l) upon electrolysis and levels off during this same course. Interestingly, the S 2p signal remains unchanged over the course of continuous activation (Table S2). Although significant changes have taken place on the surface structure, the XPS results herein indicate the Ni_3S_2@NPC retains its atomic ratio (Ni/S≈3:2) on the newly constructed superface after long-term activation (Table S2), implying the high stability of the porous Ni_3S_2 films.

An issue with the cell in Figure 3a is that the O_2 evolved on the anode can partially dissolve into the electrolyte and migrate to the cathode in the one-component cell which could affect the Ni_3S_2@NPC electrode. To avoid this, a two compartment H-cell was used with a Nafion membrane (N115) to separate the two parts (Figure S13). In this case, the electrochemical self-activation of Ni_3S_2@NPC could not be obtained as it did in the one-component cell (Figure S14). This shows that O_2 is required for the activation process. The Ni and Cu ion concentrations in the electrolyte (0.5 M H_2SO_4) during the one-component cell activation process were measured using ICP-OES analysis. Almost no copper is detected in the electrolyte; while the nickel ion concentration increases gradually upon electrolysis and levels off after one turn multi-step activation (Figure S12b), suggesting that the electrode is stable through restructuring at the surface. From the combined analyses of SEM, AFM, and XPS (an intensity increase of the Cu signal on the electrode surface upon activation), a reasonable explanation for this could be summarized as an O_2-induced dissolution-deposition activation mechanism, where the dissolved active species can be re-deposited on the electrode leading to surface rearrangement. The electropositive Cu ions that have dissolved at the electrode/electrolyte interface can be readily reduced to form new frameworks. Similarly, additional Ni and S

species could be re-introduced into the surface layers to achieve surface restructuring of the electrode. The improved HER catalytic activity of the as-prepared Ni_3S_2@NPC following multi-step CP measurements was also confirmed with a graphite-rod as the counter electrode (Figure S15), eliminating the influence of Pt on the self-improved activity. In fact, only a fairly low amount of Pt (ca. 0.5 μg cm^{-2}) can be detected by ICP-OES analysis at the surface after 5th multi-step CP activation with a Pt-rod counter electrode, which even cannot be detected by XPS analysis (Figures S11b). A comparison of the improved catalytic activity of the Ni_3S_2@NPC electrode with two different counter electrodes is also given in Figure S16. The significant enhancement of the HER catalytic activity is therefore mainly caused by the coarsened electrode surface with surface rearrangement. Similar activation behavior for the Ni_3S_2@NPC electrode was also observed in 1.0 M KOH in a one-component electrolytic cell (Figure S17), while negligible self-enhanced activation was obtained in neutral media. These observations are in consistent with a previous report that CV activation of electrochemical oxidation of Co_2P nanoparticles in alkaline media performs more efficient electrocatalytic oxygen activity than that does in neutral media.[43] It is believed that the harsh acidic/alkaline media are favourable to break strong metallic Ni-Ni bonds in Ni_3S_2, and realize surface self-assembly with the help of O_2. According to the above results, a case of O_2-assisted dissolution-deposition activation mechanism is evidently possible and proposed here. Long-term testing of the electrode in the bulk gas-evolving (H_2-O_2 gas mixture) potential region results in surface rearrangement and substantially increased HER activity.

The HER electrocatalytic performance of the Ni_3S_2@NPC after 5th multi-step CP activation (a-Ni_3S_2@NPC, as shown in Figure 3) at various pH values was investigated using a typical three-electrode configuration at room temperature. Firstly, the electrocatalytic activity of a-Ni_3S_2@NPC was performed in 0.5 M H_2SO_4 by linear sweep voltammetry (LSV) with NPC template, smooth Ni wire, and Ni@NPC as a comparison. The corresponding iR-corrected polarization curves on the four surfaces are shown in Figure 5a (see more details in Figure S18). As expected, the NPC template exhibits fairly poor activity toward HER with negligible current response up to ca.–400 mV vs. RHE, while a-Ni_3S_2@NPC shows high-performance HER activity with a low onset potential of -53.8 mV, which is much more positive than Ni@NPC (-170 mV) and smooth Ni wire (-249 mV). Taking the catalytic current density of 10 mA cm^{-2} for direct comparison, a-Ni_3S_2@NPC requires only -91.6 mV overpotential, while Ni@NPC and smooth Ni wire require an overpotential (η) of -295 and -443 mV, respectively, suggesting the superior electrocatalytic H_2-evolving activity of a-Ni_3S_2@NPC. This overpotential contrasts favorably with those previously reported for non-precious metal based HER catalysts in acidic media (Table S3). Accordingly, a-Ni_3S_2@NPC exhibits a small Tafel slope of 63.5mV dec^{-1} (Figure 5b), which is much lower compared with Ni@NPC (117.4 mV dec^{-1}) and smooth Ni wire (134.5 mV dec^{-1}), demonstrating a faster HER kinetics of a-Ni_3S_2@NPC. This value implies the HER that occurred on

a-Ni_3S_2@NPC follows a Volmer–Heyrovsky mechanism with electrochemical desorption as the rate-determining step.[44] The exchange current density (j_0) of Ni_3S_2@NPC (0.492 mA cm^{-2}) calculated from the Tafel plots by using the extrapolation method (Figure S19) is about 11.2 and 50.2 times larger than that of Ni@NPC (0.044 mA cm^{-2}) and smooth Ni wire (0.0098 mA cm^{-2}) and much larger than that obtained by other HER catalysts (Table S3). Additionally, the electrode kinetics for HER was further measured by electrochemical impedance spectroscopy (EIS), as shown in Fig. 5c. The a-Ni_3S_2@NPC (inset of Figure 5c) exhibits much lower charge transfer resistance than Ni@NPC and smooth Ni wire, confirming more favorable HER kinetics of the a-Ni_3S_2@NPC. The incorporation of S into Ni nanostructures induces significantly enhanced HER activity in comparison to the individual Ni@NPC, suggesting the synergistic effect of Ni and S for HER, similar to those reported previously for nickel sulfide based catalysts.[22,28] Moreover, the synergy between the restructuring NPC skeletons and their supported newly constructed active phases may also promote the catalytic activity of the a-Ni_3S_2@NPC. [45]

To further understand the superior HER catalytic activity of a-Ni_3S_2@NPC, the electrochemically-active surface areas (ECSA) of the prepared catalysts were measured (Figure S9), as demonstrated in Figure 3h. Briefly, the ECSA was determined through capacitance measurements by a simple cyclic voltammetry (CV) method in the non-Faradaic region of 0.10-0.20 V vs RHE (Figure S9a). Based on the measured capacitances (1/2 slope, Figure 5d), which is proportional to the effective active surface area, the C_{dl} value of a-Ni_3S_2@NPC (26.6 mF cm^{-2}) is significantly higher than that of Ni@NPC (0.775 mF cm^{-2}) and smooth Ni wire (0.035 mF cm^{-2}), suggesting much larger ECSA of a-Ni_3S_2@NPC. This result demonstrates that the large ECSA resulting from the constructional features of the a-Ni_3S_2@NPC contributes to its high catalytic activity. In addition, the turnover frequency (TOF) was also estimated as a measure of the intrinsic activity of a-Ni_3S_2@NPC (see more details in Supporting Information). As shown in Figure 5e, the TOF values of both Ni@NPC and a-Ni_3S_2@NPC, plotted against the applied potential, make it clear that a-Ni_3S_2@NPC exhibits a much higher TOF response than Ni@NPC, implying a larger active site value. To make a direct comparison with that of other catalysts, the a-Ni_3S_2@NPC show high TOF values of 0.052 H_2 s^{-1} ($\eta_{100\ mV}$); 0.235 H_2 s^{-1} ($\eta_{150\ mV}$) and 0.775 H_2 s^{-1} ($\eta_{200\ mV}$) in 0.5 M H_2SO_4. These values are superior to many recently reported work, such as $MoS_{2(1-x)}Se_{2x}/NiSe_2$,[38] Ni_2P nanoparticles,[46] CoP nanoparticles,[47] double-gyroid MoS_2[48] and MoC_x nano-octahedrons.[49]

The electrocatalytic activity of a-Ni_3S_2@NPC for HER was also investigated in 1.0 M KOH (pH=14), as shown in Figure 6a. It shows an onset overpotential as low as -30.1mV and a small Tafel slope of 67.5 mV dec^{-1}. The HER catalytic current density of 10 mA cm^{-2} is achieved at η= -60.8 mV, which is significantly more positive than the values for other non-precious metal HER catalysts in basic media (Table S4). A pH neutral electrolyte is ideal for

water splitting due to its environmental benign operating condition as well as its biocompatibility. Intriguingly, the a-Ni_3S_2@NPC exhibits excellent HER activity in neutral media as well. Figure 6b shows the polarization curve of a-Ni_3S_2@NPC in 2.0 M PBS (pH=7). To deliver current densities of 1 and 2 mA cm^{-2}, overpotentials of -161.6 and -193.0 mV, respectively, are required. Although the HER catalytic activity of a-Ni_3S_2@NPC in neutral solutions is rather lower than its performance in both acid and alkaline media (Figure 6a,c), these values still compare favorably with other noble metal-free HER catalysts reported for neutral media (Table S5). Furthermore, similar to the case in acidic solutions, the large exchange current density of a-Ni_3S_2@NPC in KOH (0.786 mA cm^{-2}) and PBS (0.0428 mA cm^{-2}) also confirmed its superior HER catalytic activity over a wide pH range (Tables S4 and S5). Notably, the HER activity of a-Ni_3S_2@NPC in an alkaline solution is comparable to the one in an acidic electrolyte. To our knowledge, such non-precious catalyst that exhibits comparable HER activity in both acidic and alkaline media is rare.

To examine the HER durability of a-Ni_3S_2@NPC, multiple cyclic voltammetric scanning was performed between 0.20 and -0.20 V vs. RHE at a scan rate of 100 mV s^{-1}. As shown in Figure 6a-c, the polarization curves of a-Ni_3S_2@NPC shows negligible degradation after 2000 continuous cycles from acidic, alkaline and neutral media, in comparison to the initial ones, implying the high stability of a-Ni_3S_2@NPC at all pH values (0-14). To further prove the stability, multi-step chronoamperometric curves for a-Ni_3S_2@NPC in pH 0-14 were measured with overpotential increasing from 0 to -800 mV versus RHE and an increment of -50 or -100 mV per 1000 s (Figure 6d). In all cases, the current remains stable over a wide potential range. The rapid current responses also indicate good mass transport and robustness of the a-Ni_3S_2@NPC electrode. For long-term controlled potential electrolysis at η = -150 mV in 0.5 M H_2SO_4, the a-Ni_3S_2@NPC exhibits ultrahigh stability, which can maintain its original catalytic activity even after 111 h of electrolysis. The compositions and 3D interconnected hierarchical porous features of the a-Ni_3S_2@NPC are essential unchanged after long-term HER test, as manifested by the XPS (Figure S11), EDX (Figure S12a), SEM (Figure S20), and TEM (Figure S21) analyses. Moreover, the a-Ni_3S_2@NPC also shows extended durability in neutral and alkaline electrolytes for 28 h test (Figure S22), even operating at harsh reaction condition with a large overpotential of -800 mV. In contrast, the activity of Ni@NPC is found to decay quickly after long-term operation in the acidic media. In addition, the generated H_2 gas was further measured quantitatively and compared carefully with the theoretically expected amount to calculate the Faradaic efficiency. The result suggests that the Faradaic efficiency is over 96.5% (Figure S23). All of the above results reveal the highly efficient and robust stability of the self-supported a-Ni_3S_2@NPC electrode. Such an enhanced catalytic performance compared with unmodified materials could be rationalized as follows. (1) The self-supported design with good substrate adhesion removes the extra electrical resistance raised by binders, leads to a better electrical connection and promotes electron transport.

(2) A mild evolution of bulk gas bubbles (H_2-O_2 gas mixture) drives *in-situ* structural rearrangement and results in a highly porous structure with exposed active edges possessing fairly high activity sites. (3) The interconnected hierarchical architectures with open channels/pores facilitate fast mass transport and electrolyte penetration and allow efficient accession of more surface area as well as active sites for electrocatalytic reaction. (4) The synergy between Ni and S, and the promoting effect of the restructuring NPC skeletons also contributes to the enhanced HER catalytic activity and high durability of the porous Ni_3S_2@NPC electrode.

3. Conclusion

In summary, a self-supported nanoporous Ni_3S_2@NPC electrode has been fabricated *in-situ* using an NPC as the template via an unusual galvanic replacement approach in Ethaline with nickel chloride and thiourea as the starting materials. The Ni_3S_2@NPC electrode exhibits high-performance catalytic activity and excellent stability for HER in water across a wide range of pH with an O_2-induced electrochemical self-activation process. The enhanced catalytic performance of Ni_3S_2@NPC mainly results from the synergy between Ni and S, the synergistic interactions between the of restructuring NPC skeletons and active phases as well as its interconnected nanoporous architectures, in which the rough active edges of the ligaments offer significantly enhanced active sites, and the porous structure promotes fast mass transport and favors more efficient utilization of active sites for HER. The *in-situ* homogeneous growth of active phases directly on the nano-ligaments of NPC (current collector) performed in Ethaline provides a facile and scalable route to prepare self-supported nanoporous catalysts with high conductivity which eliminates the contact resistance induced by use of chemical binders. Moreover, this approach has been shown to be useful for other self-supported nanoporous transition metal sulfide and phosphide based catalysts (such as Ni_xP_y, Co_2P, Co_9S_8, Co_3S_4, etc.) which could also be useful for renewable energy applications.

4. Experimental Section

Materials. Choline chloride (ChCl, 98%), ethylene glycol (EG, 99%), thiourea (CH_4N_2S, 99.5%), nickel chloride hexahydrate ($NiCl_2{\cdot}6H_2O$, 98%), zinc chloride ($ZnCl_2$, 99%), sulfuric acid (H_2SO_4, 96%) and potassium hydroxide (KOH, 99.5%) were used as received from Aladdin Ltd. (Shanghai, China) without further purification. The deep eutectic solvent (DES), Ethaline, was prepared by stirring ChCl and EG together in the molar ratio of 1:2 at 353 K until a homogeneous, colorless liquid was formed. Deionized water (18.2 MΩ cm^{-1}) was used to synthesize electrolyte solution for HER catalytic experiments.

Electrocatalyst synthesis. The NPC current collector was fabricated according to the method described previously.[50] In brief, the NPC was prepared by a facile alloying/dealloying process on Cu foil in Ethaline containing

zinc chloride at 373 K, which involves electrodepositing Zn on Cu foil to form binary Cu-Zn alloys, and followed by selective dissolution of active Zn component in surface alloys to create a 3D hierarchical bicontinuous NPC film. After the dealloying process, the as-obtained monolithic NPC was washed with acetone and deionized water to remove organic residuals, and dried by N_2 gas stream. Fabrication of nanoporous Ni_3S_2 film was carried out using a novel galvanic replacement approach from an Ethaline-based plating solution, where $NiCl_2{\cdot}6H_2O$ and thiourea serve as the Ni and S sources, respectively, and NPC serves as the sacrificial template and reducing agent. It was found that both the concentration of thiourea and galvanic reaction time play crucial role on the electrcatalytic activity of Ni_3S_2@NPC samples and the optimal preparation conditions were investigated (Figures S24 and S25). In a typical synthesis, NPC with an efficient area of 4.5 cm^{-2} was immersed in 20 mL Ethaline containing 0.10 M $NiCl_2{\cdot}6H_2O$ and 0.05 M thiourea at 353 K with 5 h for growing Ni_3S_2 on NPC.

Characterization. X-ray diffraction (XRD) patterns of the prepared samples were performed on a Rigaku D/max2200 X-ray diffractometer (Cu Kα radiation), and their corresponding surface properties were investigated by an X-ray photoelectron spectrometer (XPS, PHI 550). The morphology and elemental composition of the samples were characterized using a field emission Scanning electron microscope (SEM, NOVA NanoSEM 450) equipped with an energy-dispersive X-ray spectroscopy (EDS) system, and a transmission electron microscope (TEM, Tecnai G2 F30) with an accelerating voltage of 200kV. The topological changes of the sample during the activation process were conducted by tapping mode atomic force microscopy (AFM, SPI3800N). Raman spectra were accessed by a Renishaw Invia Plus laser Raman spectrometer (Renishaw, UK). The concentrations of Ni and Cu in electrolyte after long-term electrolysis were measured by induced coupled plasma-optical emission spectroscopy (ICP–OES, Varian 700-ES). Gas analysis was performed using a gas chromatograph (Agilent 7820A, USA).

Electrocatalytic measurements. The electrocatalytic measurements were carried out in acidic (0.5 M H_2SO_4, pH=0), neutral (0.2 M PBS pH=7) and alkaline (1.0 M KOH, pH=14) solutions using a typical three-electrode setup with 50 mL electrolyte on a CHI 760D electrochemical workstation. Before measurement, the electrolyte was bubbling by high-purity H_2 for at least 30 minutes to remove residual O_2. The as-prepared Ni_3S_2@NPC was used as the working electrode; a Ag/AgCl (saturated 3.0 M KCl) was used as the reference electrode and a Pt rod (surface area = 0.32 cm^2) or a graphite rod (surface area = 6.0 cm^2) was served as the counter electrode. Linear sweep voltammetry (LSV) measurement was carried out at a scan rate of 2 mV s^{-1}. All the potentials vs. Ag/AgCl were converted to the reversible hydrogen electrode (RHE) by a typical CV measurement. In brief, the calibration was conducted in an H_2-saturated electrolyte (0.5 M H_2SO_4), with a Pt disc electrode (Φ = 4 mm) and a Pt rod using as the working and counter electrodes, individually. Figure S26 defined the mean value of the two potentials at which

the current crossed zero as the thermodynamic potential for HER. Thus, the potentials with respect to RHE should be, in 0.5 M H_2SO_4, $E_{RHE} = E_{Ag/AgCl} + 0.208$ V, in 2.0 M phosphate buffered saline (PBS), $E_{RHE} = E_{Ag/AgCl} + 0.622$ V, and 1.0 M KOH, $E_{RHE} = E_{Ag/AgCl} + 1.035$ V.

Acknowledgements

The authors gratefully acknowledge the financial support of the National Natural Science Foundation of China (51464028, 51204080, and 5177010886), the Application Foundation Research of Yunnan Province (2014FB125), and the Independent Research Funds for the State Key Laboratory (CNMRCUTS1601).

Supporting information

Characterization details and computational methods are included as Supporting information.

References

[1] S. Chu, A. Majumdar, Nature 488 (2012) 294-303.

[2] S. Cobo, J. Heidkamp, P.A. Jacques, J. Fize, V. Fourmond, L. Guetaz, B. Jousselme, V. Ivanova, H. Dau, S. Palacin, Nat. Mater. 11 (2012) 802-807.

[3] T.R. Cook, D.K. Dogutan, S.Y. Reece, Y. Surendranath, T.S. Teets, D.G. Nocera, Chem. Rev. 110 (2010) 6474-6502.

[4] M.S. Dresselhaus, I.L. Thomas, Nature 414 (2001) 332-337.

[5] J. Chow, R.J. Kopp, P.R. Portney, Science 302 (2003) 1528-1531.

[6] D.G. Nocera, Acc. Chem. Res. 45 (2012) 767-776.

[7] J.A. Turner, Science 305 (2004) 972-974.

[8] H.B. Gray, Nat. Chem. 1 (2009) 7-7.

[9] J. Tian, Q. Liu, A.M. Asiri, X. Sun, J. Am. Chem. Soc. 136 (2014) 7587-7590.

[10] C.C.L. McCrory, S. Jung, I.M. Ferrer, S.M. Chatman, J.C. Peters, T.F. Jaramillo, J. Am. Chem. Soc. 137 (2015) 4347-4357.

[11] X. Wang, Y.V. Kolen'ko, X.Q. Bao, K. Kovnir, L. Liu, Angew. Chem. Int. Ed. 54 (2015) 8188-8192.

[12] M.G. Walter, E.L. Warren, J.R. McKone, S.W. Boettcher, Q.X. Mi, E.A. Santori, N.S. Lewis, Chem. Rev. 110 (2010) 6446-6473.

[13] Z. Pu, Q. Liu, A.M. Asiri, Y. Luo, X. Sun, Y. He, Electrochim. Acta 168 (2015) 133-138.

[14] A. Kundu, J.N. Sahu, G. Redzwan, M.A. Hashim, Int. J. Hydrog. Energy 38 (2013) 1745-1757.

[15] J.W.D. Ng, M. García-Melchor, M. Bajdich, P. Chakthranont, C. Kirk, A. Vojvodic, T.F. Jaramillo, Nat. Energy 1 (2016) 16053.

[16] Z. Peng, D. Jia, A.M. Al-Enizi, A.A. Elzatahry, G. Zheng, Adv. Energy Mater. 5 (2015) 1402031.

[17] X. Zou, X. Huang, A. Goswami, R. Silva, B.R. Sathe, E. Mikmeková, T. Asefa, Angew. Chem. Int. Ed. 126 (2014) 4461-4465.

[18] J. Tian, Q. Liu, A.M. Asiri, X. Sun, J. Am. Chem. Soc. 136 (2014) 7587-7590.

[19] Y.Y. Ma, C.X. Wu, X.J. Feng, H.Q. Tan, L.K. Yan, Y. liu, Z. Kang, E. Wang, Y.G. Li, Energy Environ. Sci. (2017).

[20] M.A. McArthur, L. Jorge, S. Coulombe, S. Omanovic, J. Power Sources 266 (2014) 365-373.

[21] S. Gupta, N. Patel, R. Fernandes, R. Kadrekar, A. Dashora, A.K. Yadav, D. Bhattacharyya, S.N. Jha, A. Miotello, D.C. Kothari, Appl. Catal. B: Environ. 192 (2016) 126-133.

[22] L. Mi, Q. Ding, W. Chen, Z. Zheng, H. Hou, C. Liu, C. Shen, RSC Adv. 2 (2012) 6817-6823.

[23] L.L. Feng, G. Yu, Y. Wu, G.D. Li, H. Li, Y. Sun, T. Asefa, W. Chen, X. Zou, J. Am. Chem. Soc. 137 (2015) 14023-14026.

[24] J. Yu, F.X. Ma, Y. Du, P.P. Wang, C.Y. Xu, L. Zhen, ChemElectroChem 4 (2017) 594-600.

[25] J.L Lv, T.X. Liang, J. Solid State Chem. 243 (2016) 106-110.

[26] W. Zhou, X.J. Wu, X. Cao, X. Huang, C. Tan, J. Tian, H. Liu, J. Wang, H. Zhang, Energy Environ. Sci. 6 (2013) 2921-2924.

[27] Z. Cui, Y. Ge, H. Chu, R. Baines, P. Dong, J. Tang, Y. Yang, P. M. Ajayan, M. Ye, J. Shen, J. Mater. Chem. A 5 (2017) 1595-1602.

[28] Y. Wu, G.D. Li, Y. Liu, L. Yang, X. Lian, T. Asefa, X. Zou, Adv. Funct. Mater. 26 (2016) 4839-4847.

[29] N. Jiang, L. Bogoev, M. Popova, S. Gul, J. Yano, Y. Sun, J. Mater. Chem. A 2 (2014) 19407-19414.

[30] C. Tang, Z.H. Pu, Q. Liu, A.M. Asiri, Y.L. Luo, X.P. Sun, Int. J. Hydrog. Energy 40 (2015) 4727-4732.

[31] T.W. Lin, C.J. Liu, C.S. Dai, Appl. Catal. B: Environ. 154-155 (2014) 213-220.

[32] W. Zhu, X. Yue, W. Zhang, S. Yu, Y. Zhang, J. Wang, J. Wang, Chem. Commun. 52 (2016) 1486-1489.

[33] B. You, Y. Sun, Adv. Energy Mater. 6 (2016) 1502333.

[34] C. Yang, Q.B. Zhang, A.P. Abbott, Electrochem. Commun. 70 (2016) 60-64.

[35] J.H. Wang, Z. Cheng, J.L. Bredas, M. Liu, J. Chem. Phys. 127 (2007) 214705 1-8.
[36] N. Jiang, Q. Tang, M. Sheng, B. You, D.-e. Jiang, Y. Sun, Catal. Sci. Technol. 6 (2016) 1077-1084.
[37] E.L. Smith, A.P. Abbott, K.S. Ryder, Chem. Rev. 114 (2014) 11060-11082.
[38] H. Zhou, F. Yu, Y. Huang, J. Sun, Z. Zhu, R.J. Nielsen, R. He, J. Bao, W.A. Goddard Iii, S. Chen, Z. Ren, Nat. Commun. 7 (2016) 12765.
[39] Q. Hu, G. Li, J. Pan, L. Tan, J. Lu, L. Zhuang, Int. J. Hydrog. Energy 38 (2013) 16264-16268.
[40] J.G. Wang, D. Jin, R. Zhou, C. Shen, K. Xie, B. Wei, J. Power Sources 306 (2016) 100-106.
[41] H. Chen, J. Jiang, Y. Zhao, L. Zhang, D. Guo, D. Xia, J. Mater. Chem. A 3 (2015) 428-437.
[42] D.J. Aston, D.J. Payne, A.J.H. Green, R.G. Egdell, D.S.L. Law, J. Guo, P.A. Glans, T. Learmonth, K.E. Smith, Phys. Rev. B 72 (2005).
[43] K. Xu, H. Cheng, L. Liu, H. Lv, X. Wu, C. Wu, Y. Xie, Nano Lett. 17 (2017) 578-583.
[44] Z. Chen, D. Cummins, B.N. Reinecke, E. Clark, M.K. Sunkara, T.F. Jaramillo, Nano Lett. 11 (2011) 4168-4175.
[45] Y. Liu, Q. Li, R. Si, G.D. Li, W. Li, D.P. Liu, D. Wang, L. Sun, Y. Zhang, X. Zou, Adv. Mater. (2017) 1606200.
[46] E.J. Popczun, J.R. McKone, C.G. Read, A.J. Biacchi, A.M. Wiltrout, N.S. Lewis, R.E. Schaak, J. Am. Chem. Soc. 135 (2013) 9267-9270.
[47] E.J. Popczun, C.G. Read, C.W. Roske, N.S. Lewis, R.E. Schaak, Angew. Chem. Int. Ed. 53 (2014) 5427-5430.
[48] J. Kibsgaard, Z. Chen, B.N. Reinecke, T.F. Jaramillo, Nat. Mater. 11 (2012) 963-969.
[49] H.B. Wu, B.Y. Xia, L. Yu, X.Y. Yu, X.W. Lou, Nat. Commun. 6 (2015) 6512.
[50] C. Yang, Q.B. Zhang, M.Y. Gao, Y.X. Hua, C.Y. Xu, J. Electrochem. Soc. 163 (2016) D469-D475.

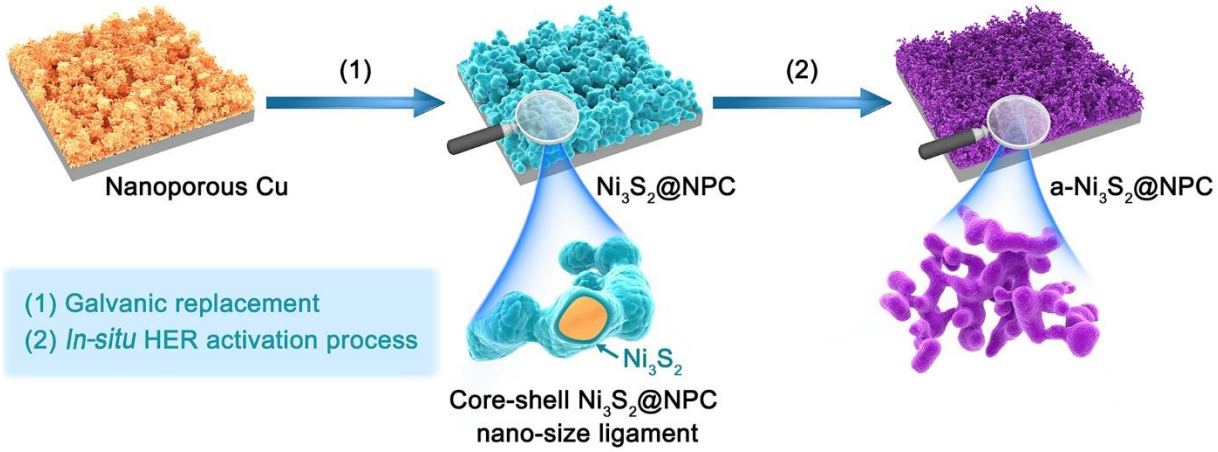

Scheme 1. Schematic illustration showing the fabrication process of the nanoporous Ni_3S_2@NPC electrode and its *in-situ* activation process during HER electrolysis.

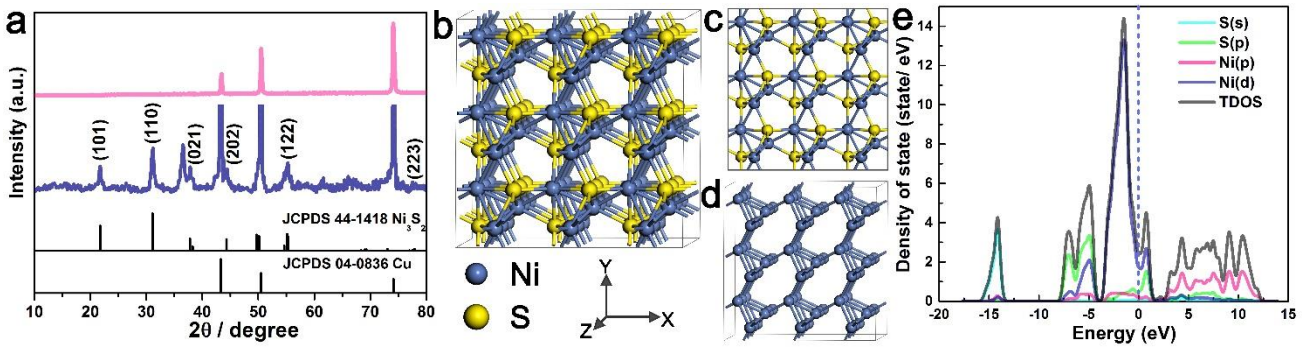

Figure 1. (a) XRD patterns of bare NPC (pink line) and Ni_3S_2@NPC (navy line), which was synthesized from Ethaline containing 0.1 M $NiCl_2 \cdot 6H_2O$ and 0.05 M thiourea at 353 K for 5 h. (b-c) front and top view of Ni_3S_2 supercell (3×3×3) shows the crystal structure, (d) Network of Ni-Ni bond paths in heazlewoodite Ni_3S_2 crystallizes obtained by deleting all of the S atoms. (e) The corresponding electronic density of states of total (TDOS) and the partial signals for S(s), S(p), Ni(p) and Ni(d).

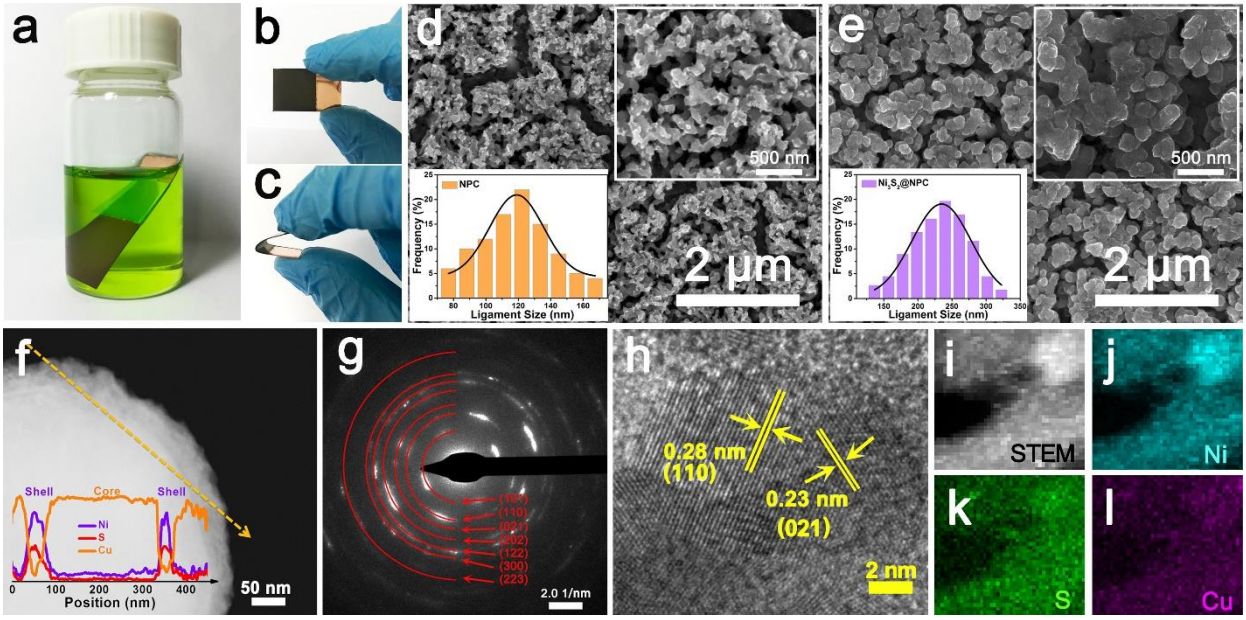

Figure 2. (a) Photographic image shows the galvanic replacement reaction operated in a glass vial by immersion of an NPC template in Ethaline containing $NiCl_2 \cdot 6H_2O$ and thiourea. (b and c) Images of the as-prepared Ni_3S_2@NPC during bending tests. (d-e) Typical top-view SEM images of the NPC template and Ni_3S_2/NPC sample, inset: the corresponding ligament size histogram and magnification images. (f) HAADF-STEM image and compositional line profiles across the single nano-ligament along the line marked by an arrow. (g) The corresponding SAED pattern of Ni_3S_2@NPC, indicating the Ni_3S_2@NPC with polycrystalline structure. (h) HR-TEM image of Ni_3S_2@NPC sample. (i) STEM image. (j-l) Corresponding EDS mapping of Ni, S and Cu for the Ni_3S_2@NPC sample.

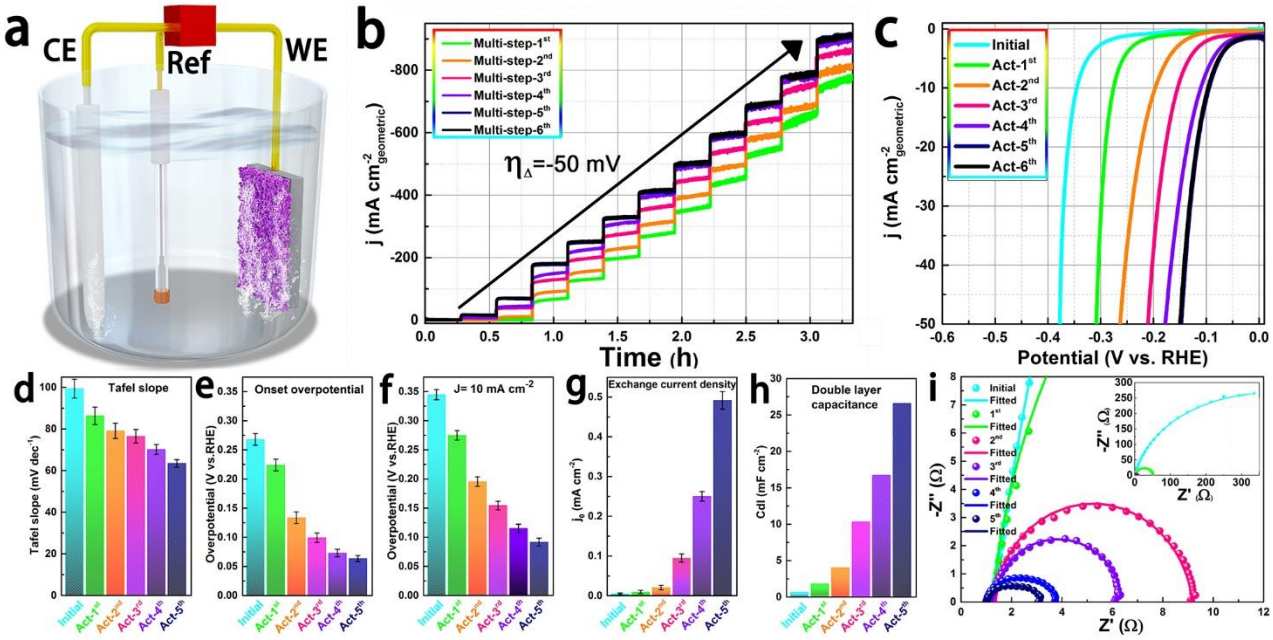

Figure 3. (a) Schematic diagram of *in-situ* HER activation device. (b) Consecutive multi-step chronoamperopmetric tests for Ni_3S_2@NPC in 0.5 M H_2SO_4 at various overpotentials, from -100 mV to -650 mV with an increment of -50 mV at each stage (1000s). (c) Polarization curves of Ni_3S_2@NPC at varying stages of the activation process. (d) Tafel slope. (e) Onset potential. (f) Overpotential required for j=10 mA cm^{-2}. (g) Exchange current density and (h) Double layer capacitance of Ni_3S_2@NPC at different self-activation stages. (i) Nyquist plots of Ni_3S_2@NPC in 0.5 M H_2SO_4 at an overpotential of -150 mV at different degrees of activation (from initial to 5^{th} act).

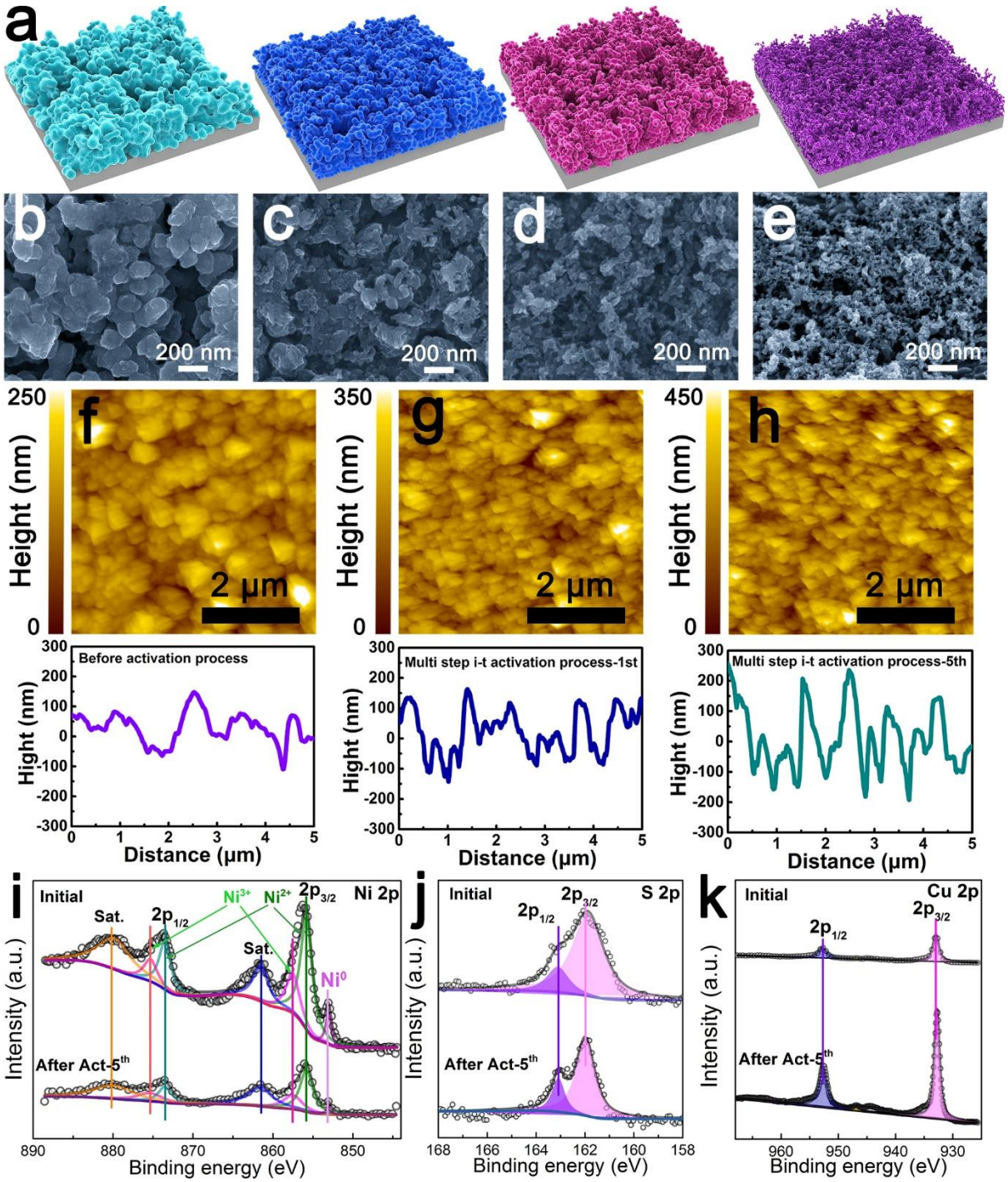

Figure 4. (a) Schematic diagrams of Ni_3S_2@NPC showing the structure changes during operando self-enhanced activation process. (b-e) Representative SEM images of initial, act-1st, act-2nd and act-5th samples. AFM images and corresponding line scans for Ni_3S_2@NPC film at different activation stages (f: initial, g: act-1st, and h: act-5th). (i-k) XPS spectra of Ni2p, S2p and Cu2p for Ni_3S_2@NPC before and after act-5th process.

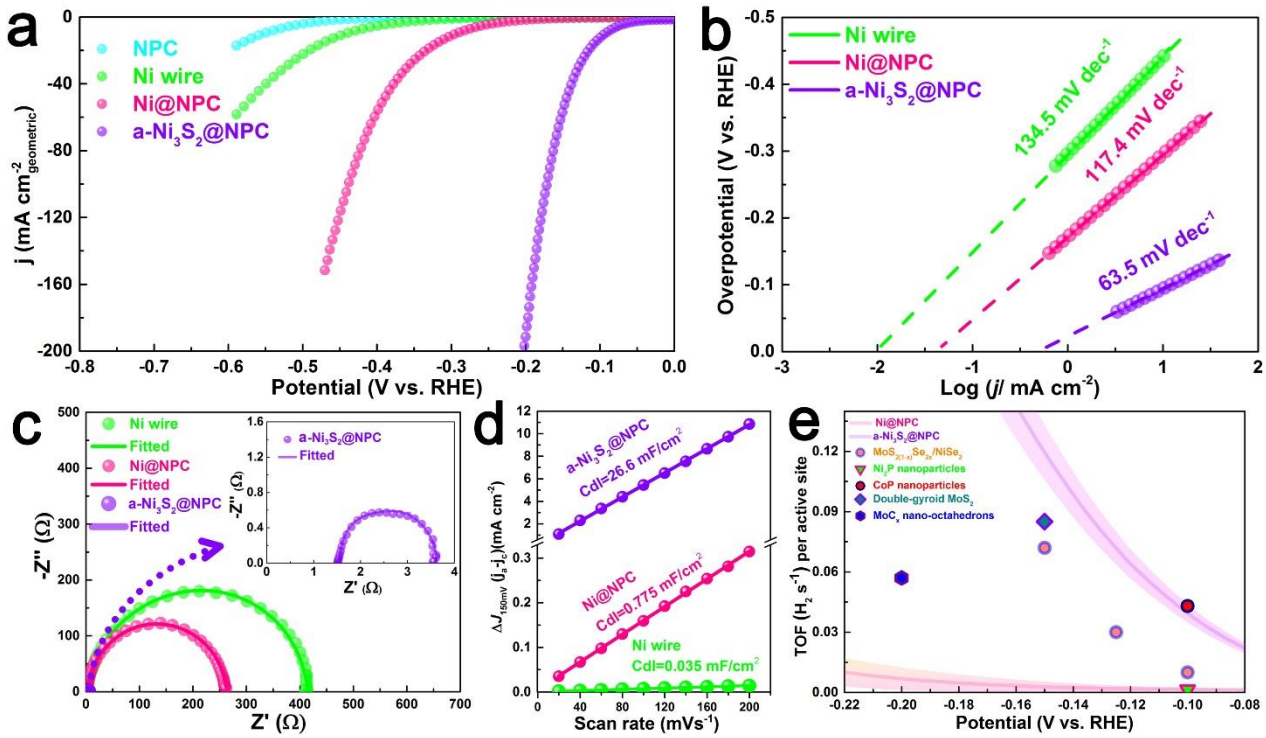

Figure 5. (a) Polarization curves for NPC, Ni wire, Ni@NPC and a-Ni_3S_2@NPC in 0.5 M H_2SO_4 at a scan rate of 2 mV s^{-1} (iR-corrected). (b) The corresponding Tafel slope plots derived from (a). (c) Nyquist plots of Ni wire, Ni@NPC and a-Ni_3S_2@NPC in 0.5 M H_2SO_4 at an overpotential of -150 mV. (d) The current density against scan rate of smooth Ni wire, Ni@NPC and a-Ni_3S_2@NPC at 0.15 V vs. RHE, $\Delta j_{150mV}(j_a\text{-}j_c)$. (e) TOF curves of Ni@NPC and Ni_3S_2@NPC together with $MoS_{2(1-x)}Se_{2x}/NiSe_2$,[38] Ni_2P nanoparticles,[44] CoP nanoparticles,[47] Double-gyroid MoS_2[48] and MoC_x nano-octahedrons.[49] The solid line represents a typical TOF value calculated using 39.1 μF cm^{-2} as the specific capacitance standard, and the borders of the colored gradients represent using 20 and 60 μF cm^{-2} for a lower and upper limit.

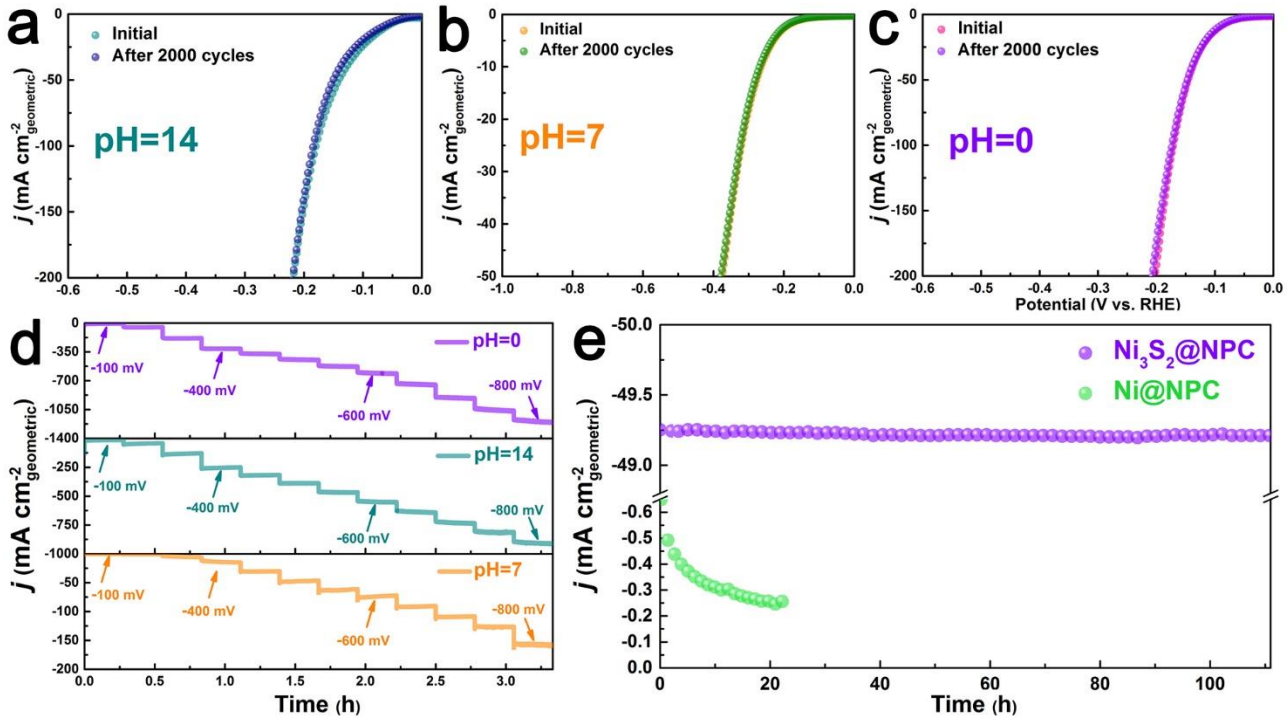

Figure 6. (a-c) Polarization curves of a-Ni_3S_2@NPC in alkaline (1.0 M KOH, pH=14), neutral (2.0 M PBS, pH=7), and acidic (0.5 M H_2SO_4, pH=0) solutions before and after 2000 CV cycles. (d) Multi-step chronoamperometric curves for a-Ni_3S_2@NPC in 0.5 M H_2SO_4, 1.0 M KOH, and 2.0 M PBS, respectively. The overpotential initials at -100 mV and ends at -800 mV, with an increment of 50 or 100 mV every 1000s. (e) Time-dependent current density curves for Ni@NPC and a-Ni_3S_2@NPC in 0.5 M H_2SO_4 at an overpotential of -150 mV (without iR correction).